Fracture process analysis in Magnesia-Hercynite refractory materials by combining an enhanced Digital Image Correlation method with Wedge Splitting Test

Imad Khlifi, Octavian Pop, J.C. Dupré, Pascal Doumalin, Marc Huger

To be submitted in Journal of theoretical and applied fracture mechanics

Fracture process analysis in Magnesia-Hercynite refractory materials by combining an enhanced Digital Image Correlation method with Wedge Splitting Test

Imad Khlifi [1], Octavian Pop[2], Jean-Christophe Dupré[3], Pascal Doumalin[3], Marc Huger [1],

[1] IRCER - UMR CNRS 7315, CEC, 12 rue Atlantis, 87068 Limoges Cedex France

[2] GC2D, 17 Boulevard Jacques Derche, 19300 Egletons Cedex France

[3] Institut Pprime, UPR CNRS 3346, 11 Boulevard Marie et Pierre Curie, 86962 Futuroscope Chasseneuil Cedex France

ABSTRACT

Magnesia-Hercynite bricks destined for thermal shock applications in cement rotary kilns often show an enhanced crack propagation resistance due to an engineered microstructure design. In these materials, microcrack networks, resulting from the thermal expansion mismatch between magnesia matrix and Hercynite aggregates, promote the activation of energy dissipating mechanisms within the so-called Fracture Process Zone (FPZ) during loading. In this research, the fracture behaviour of a Magnesia-Hercynite material has been investigated by coupling an enhanced Digital Image Correlation method (2P-DIC) with the Wedge Splitting Test (WST). The coupling of these advanced characterisation methods is very effective in measuring important fracture parameters accurately and in highlighting characteristic fracture mechanisms, such as crack-branching. A refined R-curve approach is proposed with effective fracture energy calculations based on 2P-DIC measurements. The results demonstrate interesting correlations between FPZ development and an enhanced crack propagation resistance.

KEY-WORDS: Refractories, Magnesia-Hercynite, Thermal shock resistance, Fracture behaviour, Fracture process zone, Digital image correlation

LIST OF SYMBOLS

$\mathbf{F_V}$ vertical load

$\mathbf{F_H}$ horizontal load

$\mathbf{F_{H\,max}}$ maximum horizontal load

$\boldsymbol{\delta_V}$ vertical displacement

$\boldsymbol{\delta_H}$ horizontal displacement or crack opening displacement

$\boldsymbol{\delta_{Hmax}}$ maximum crack opening

A projected fracture area

α angle of the wedge

b width of the sample

h height of the sample

y vertical distance between the loading-point and the centre of gravity of the fracture area.

$\boldsymbol{\sigma_{NT}}$ nominal notch tensile strength

G_T total fracture energy

G_{el} elastic energy

G_f specific fracture energy

I_i grey level of each pixel in the mark tracking method

I_s threshold defined by the user in the mark tracking method

Φ material transformation function

$\mathbf{q}$ local transformation vector

C correlation coefficient in DIC

$\bar{f}_D$ average grey level values on subset D in the reference image

$\bar{g}_D$ average grey level values on subset D in the deformed image

$C_{XC}(\underline{X_c, \theta, Q})$ correlation coefficient in 2P-DIC

X_C horizontal position of discontinuity in subset

θ orientation of discontinuity boundary

n horizontal dimension of subsets

m vertical position of subsets

ε pseudo-strain threshold

$L_{eq,i}$ equivalent crack length measured by 2P-DIC at a specific loading state i

$L_{eff,i}$ cumulated damage length measured by 2P-DIC at a specific loading state i

$G_{eq,i}$ equivalent fracture energy measured at a specific loading state i

$G_{eff,i}$ effective fracture energy measured at a specific loading state i

ACRONYMS

CTE coefficient of thermal expansion

WST Wedge Splitting Test

FPZ Fracture Process Zone

COD Crack Opening Displacement

DIC Digital Image Correlation

2P-DIC Two-Parts Digital Image Correlation

ROI Region Of Interest

SEM Scanning Electron Microscope

I. INTRODUCTION

Magnesia based refractories are used as a lining in rotary kilns that serve to produce cement. These materials are frequently subjected to mechanical stresses induced by thermal cycling and thermal shocks. The latter can lead to critical stresses and induce a premature refractory failure if the material exhibits a brittle behaviour, which is the case for most ceramics. In fact, the thermal shock resistance of refractories has been frequently linked with crack propagation resistance ([1,2]. Moreover, it has been shown that deviations from a purely linear elastic mechanical behaviour can lead to a reduction in refractory brittleness, and thus improve crack propagation resistance [3–5]. Materials with a non-linear mechanical behaviour are characterized by their ability for strain accommodation, usually at the expense of strength. In this sense, the microstructure of refractories can be tailored in order to promote energy dissipating mechanisms by adjusting the composition, in particular aggregate size and shape [6]. The main mechanisms that operate within the Fracture Process Zone (FPZ) during crack propagation in a typical refractory material are microcrack toughening [7,8] and bridging mechanisms [9]. The interaction of these mechanisms has an important impact on FPZ development and elastic energy dissipation [10]. Moreover, key microstructure-property design criteria have been defined in order to promote the development of a fracture process zone, entailing increased elastic energy consumption and reducing brittleness [11].

The occurrence of these phenomena in magnesia-spinel refractories can be encouraged by promoting the development of a network of microcracks. This network of microcracks, developed as a result of the coefficient of thermal expansion (CTE) mismatch between refractory constituents, leads to Facture Process Zone (FPZ) development [12]. Indeed, the difference in thermal expansion between Magnesia and Hercynite favours microcracking [13] during cooling after sintering, which in turn induces a peculiar thermomechanical behaviour [14]. It has been shown in previous studies that MgO-$MgAl_2O_4$ materials exhibit a better thermal shock resistance [15] and a non-linear mechanical behaviour thanks to the CTE mismatch between the magnesia matrix and the spinel inclusions [16–18].

In relation with refractory microstructure-property design criteria, the effective fracture energy of refractories is an important fracture parameter that may be used to characterise crack propagation resistance and thus, the thermal shock resistance [19]. However, the surface energy used in Griffith's approach for brittle materials is not valid for refractory materials. In fact, the surface energy is based on thermodynamic calculations relating to Gibbs free energy, which is associated with the creation of a smooth crack surface. Using this energy as a fracture criterion would mean disregarding crucial energy dissipating mechanisms occurring in refractories, such as microcracking and crack tortuosity at the microscopic scale, as well as other phenomena. Therefore, there is a clear need for the measurement of the effective fracture energy based on appropriate fracture tests using convenient analysis methods. In this regard, it is important to ensure a stable fracture when performing fracture tests. This is particularly difficult to achieve in brittle and quasi-brittle materials since the elastic energy usually stored by the loading machine-sample system is released abruptly, breaking the sample in two halves. The most effective ways to circumvent this problem include reducing the elastic energy stored in the loading device and performing tests on pre-notched samples. Given the quasi-brittle nature of refractories and the associated development of a FPZ, experimental considerations must be taken about the fracture surface to specimen volume ratio. This ratio should be high enough in order to ensure that the FPZ is fully developed and not confined during the fracture test. In fact, the size effect has many implications including the validity of fracture energy values measured using common fracture tests [20,21]. Nevertheless, thanks to large volume test specimens, fracture tests such as the compact tension and the wedge-splitting test offer a more representative area for crack propagation

while, at the same time, promoting a stable fracture. The latter has been applied by numerous researchers to characterize the fracture behaviour of concrete and refractories [11,22].

Using one of the aforementioned fracture tests, the so-called resistance curves (R-curves) can be calculated. These R-curves give an insight on the influence of FPZ development on the fracture behaviour, which is a key information in the design of refractories with an enhanced crack propagation resistance. Indeed, from [23], the theoretical evolution of an R-curve as a function of crack length shows the impact of FPZ extension through the successive development of the frontal zone and the wake region. The interaction of the main crack with the microcracked frontal zone leads to an initial increase of the R-curve, which is followed by a more significant increase once the wake region is fully developed, before a plateau-like region is reached. The development of the FPZ during the fracture of refractories, and some ceramics, has been associated with a rising R-curve concept, where the crack propagation resistance of the material increases with crack length [24,25]. Experimental R-curves are determined from load-displacement curves of fracture test results, numerous methods have been developed [26–28] to evaluate the essential fracture parameters that describe the fracture process, namely crack length and fracture energy.
The R-curve behaviour and energy dissipating mechanisms have been considered in an extension of Hasselman's thermal shock theory [29], where an expression has been defined to estimate the final crack size from fracture energies. Nevertheless, the full extent of energy dissipating mechanisms' effectiveness within a specific FPZ remains largely unexplored due to the complexity of mechanism interactions and other phenomena [30].

Appropriate experimental characterization of fracture is essential for the understanding of important fracture mechanisms and their impact on the fracture behaviour of refractories. Therefore, to improve understanding of mechanisms driving FPZ extension during fracture tests, advanced experimental tools such as Digital Image Correlation (DIC) could be employed to provide accurate monitoring of crack propagation. DIC has been applied in many fracture characterization studies involving different materials [31–33], including refractories [34–36]. The evaluation of strain fields during cracking is marked by uncertainties and leads to an approximate assessment of crack features. Indeed, disturbances of the measured displacement field and the subsequently calculated strain field are caused by discontinuities crossing subsets within the investigated area (i.e no continuity of the optical flow is ensured in this case) [37]. These perturbations hinder not only the determination of the displacement field, but also crack position and length, which are essential features of fracture mechanics. These limitations, induced by fracture, come from the kinematic assumptions of DIC, which are comprised in the framework of continuum mechanics. Therefore, an adaptation of classical DIC methods is necessary to address problems in the fracture mechanics. Many DIC methods have thus been adapted to account for such discontinuities during the calculations, including the 2P-DIC method [38] which is used in this study.

The following article details a novel fracture analysis method based on the application of the Wedge Splitting Test combined with advanced Digital Image Correlation processing (2P-DIC) in order to measure damage length and effective fracture energies of Magnesia-based refractories.

II. MATERIALS AND EXPERIMENTAL METHODS

II.1. Magnesia-Hercynite model refractory materials

In the present study, model materials, composed of Magnesia and Hercynite, have been investigated in order to understand the impact of energy dissipating mechanisms on FPZ development and the fracture behaviour. In order to better understand the phenomena taking place during fracture,

simplified compositions of two types of refractories have been elaborated, namely pure Magnesia and Magnesia-Hercynite.

On one hand, a pure Magnesia brick (MgO) composed of sintered magnesia raw material with a purity of over 98% has been produced. Fine particles (<1 mm) and aggregates (<5 mm) are used for the elaboration of the magnesia brick. The granulometric distribution was optimised to improve pressing conditions. The powder and aggregates are mixed then pressed using a nominal pressure of 120 MPa. Then, the brick is sintered at a temperature around 1600°C.

On the other hand, the Magnesia-Hercynite brick (MH5) has been produced by adding 5 wt. % of Hercynite aggregates (1-3 mm) to the Magnesia mix, which is composed of both fine particles and aggregates. In the following, monophasic magnesia (both aggregates and fine particles) will be referred to as the matrix while the Hercynite, introduced in the form of aggregates, will be called inclusions. In microstructure design, this vocabulary relates to a model composite approach where Hercynite, introduced as an inclusion, induces energy dissipating mechanisms that have an impact on refractory fracture behaviour.

Physical properties of the two studied materials have been measured and reported in Table 1.

Table 1 : Physical properties of pure MgO brick and MH5

Bricks	Composition		Bulk density (g/cm^3)	Porosity (%)	Young's modulus at room temperature
	MgO (Matrix)	$FeAl_2O_4$ (Aggregate)			
MgO	100%	_	2.98	14.3 %	85 GPa
MH5	95%	5%	2.95	15.4 %	33 GPa

Moreover, the thermal expansion of MgO and hercynite has been measured up to 1350 °C using a heating rate of 5°C/min. As indicated in Table 2, the CTE of magnesia is much higher than that of hercynite both in low temperature range (200-400 °C) and high temperature range (1000-1200 °C).

Table 2 : Summary of measured CTE values for magnesia and hercynite during heating

Material	Coefficient of thermal expansion (10^{-6} °C^{-1})	
	200-400 °C	1000-1200 °C
Magnesia	13.2	16.3
Hercynite	8.7	11.7

II.2. The Wedge Splitting Test

The Wedge Splitting Test (WST) offers an ideal configuration to achieve stable crack propagation in heterogeneous coarse-grained materials, including refractories. Thanks to this type of test, it is possible to measure fracture parameters such as the nominal notch tensile strength (σ_{NT}) and the specific fracture energy (G_f).

In order to perform the WST, cubic refractory samples of 100x100x100 mm^3 have been machined with a groove on top surface, which holds the loading setup, and a 2.5 mm wide notch for crack initiation. The dimensions of the groove and the notch are 24x22x100 mm^3 and 3.5x12x100 mm^3 respectively. The loading setup for the WST comprises four load transmission pieces (rolls + supports), a wedge for vertical load application and a linear support placed at the bottom of the sample, as schematised in Figure 1.

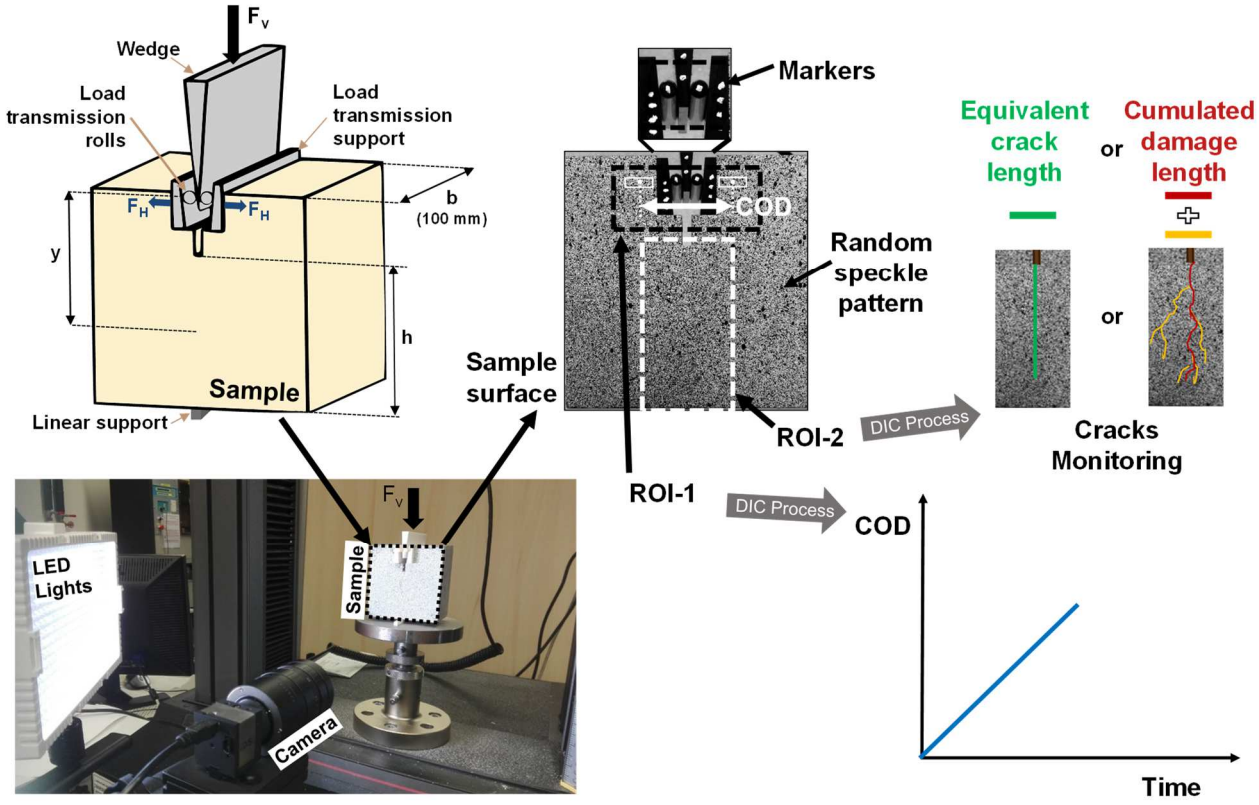

Figure 1: WST setup including sample geometry with loading conditions, markers on metallic loading parts, random speckle pattern on lateral sample surface, images acquisition and final DIC treatment on two Regions Of Interest: ROI-1 for measuring Crack Opening Displacement (COD) by classical DIC and ROI-2 for monitoring crack propagation within FPZ by 2P-DIC.

Thanks to load transmission parts on top of the sample, the vertical load, F_V, applied to the wedge is converted into horizontal loads, F_H, which are finally applied to the sample. The horizontal load can be calculated from the vertical load and the angle of the wedge ($\alpha = 10°$), according to equation (1).

$$F_H = \frac{F_V}{2.\tan\left(\frac{\alpha}{2}\right)} \quad (1)$$

In the same way, horizontal displacements, corresponding to the Crack Opening Displacement (δ_H or COD), can be calculated from the vertical displacement of the crosshead, or the wedge (δ_V) using the following equation (2).

$$\delta_H = 2.\delta_V.\tan(\alpha/2) \quad (2)$$

This setup, made of very rigid parts, contributes to limiting the elastic energy stored in the testing machine and thus promotes stable crack propagation.

A nominal notch tensile strength can be calculated from the maximum load and specimen dimensions using the following equation:

$$\sigma_{NT} = \frac{F_{H\,max}}{b.h} + \frac{6F_{H\,max}.y}{b.h^2} \quad (3)$$

Where $F_{H\,max}$ is the maximum horizontal load, b and h are the width and the height of the fracture surface and y the vertical distance between the loading-point and the centre of gravity of the fracture area.

Moreover, the total fracture energy can be calculated from the total area under the horizontal load-δ_H curve according to the following integral.

$$G = \frac{1}{A}\int_0^{\delta_{H\max}} F_H \, . \, d\delta_H \quad (4)$$

Where A is the projected fracture area, δ_H the crack opening displacement and $\delta_{H\max}$ represents the maximum crack opening value during the experiment. For practical reasons, the fracture energy is calculated up to 15% of the maximum δ_H as shown in Figure 2.

Given that fracture is not completely reached at 15% of the maximum load, some residual elastic energy is expected to be stored in the sample and included in the total energy. This elastic energy can be calculated at each state during loading by assuming an elastic material behaviour, following equation.

$$G_{el} = \frac{1}{2} . F_H . \delta_H \quad (5)$$

Hence the specific fracture energy, G_f, corresponds to the difference between G_T and G_{el} ($G_f = G_T - G_{el}$). This term relates to the energy consumed by the fracture process zone during crack propagation.

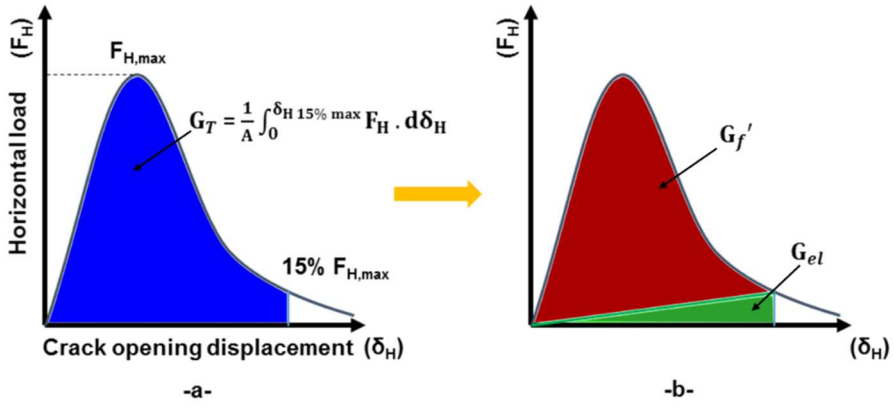

Figure 2: Typical Horizontal load-δ_H curve and area under the curve corresponding to:
a) total energy and b) decomposition of total energy into fracture (red) and elastic (green) energies.

The accurate measurement of the horizontal load and δ_H is a key point during WST experiments. Even if it would appear rather simple, the valuation the δ_H (COD) from the crosshead displacement is in fact usually prone to significant parasitic effects which lead to inaccurate values. Thus, in the present study, alternative approaches will be proposed to reduce these experimental artefacts by using optical methods. Moreover, a refined DIC method will be used to accurately monitor the fracture process throughout the sample during experiments at room temperature.

II.3. Wedge Splitting test monitoring by optical techniques

The use of optical methods during the Wedge Splitting Test (WST) offers a rich panel of analytical tools. These tools have been used to evaluate the loading conditions (by Mark Tracking technique), to determine the boundary conditions and displacement fields (by Digital Image Correlation) and to measure the crack opening and length (by an adapted Digital Image Correlation method). In order to do this, the WST sample was prepared for the DIC matching process by first spraying an opaque black layer over the surface followed by droplets of white paint, some markers were then drawn on the loading metallic parts. As shown in Figure 1, a CMOS USB camera with a resolution of 2560x1920 px^2 was placed in front of a prepared WST sample while LED lights were used as a cold light source to provide sufficient illumination without heating the sample. The acquired images were then processed using the DIC software and marker tracking software.

II.3.a. Load transmission "part" monitoring by Mark Tracking method

Mark Tracking (MT) method may be used as a convenient way to fully monitor WST setup displacements and determine the crack opening displacement accurately. This non-contact optical

method has been mainly used for local displacement and strain measurements [39,40]. It is particularly well adapted for the monitoring of the boundary conditions of mechanical tests [41]. One simply needs to draw as many marker points, on the sample or loading device, as necessary for the measurement. Thus, each marker point can be followed to obtain displacements. Moreover, a high contrast between the markers and the support on which they will be defined, needs to be achieved in order to perform accurate measurements (i.e: White markers on black background or vice versa). The principle of Mark Tracking method is illustrated in Figure 3.

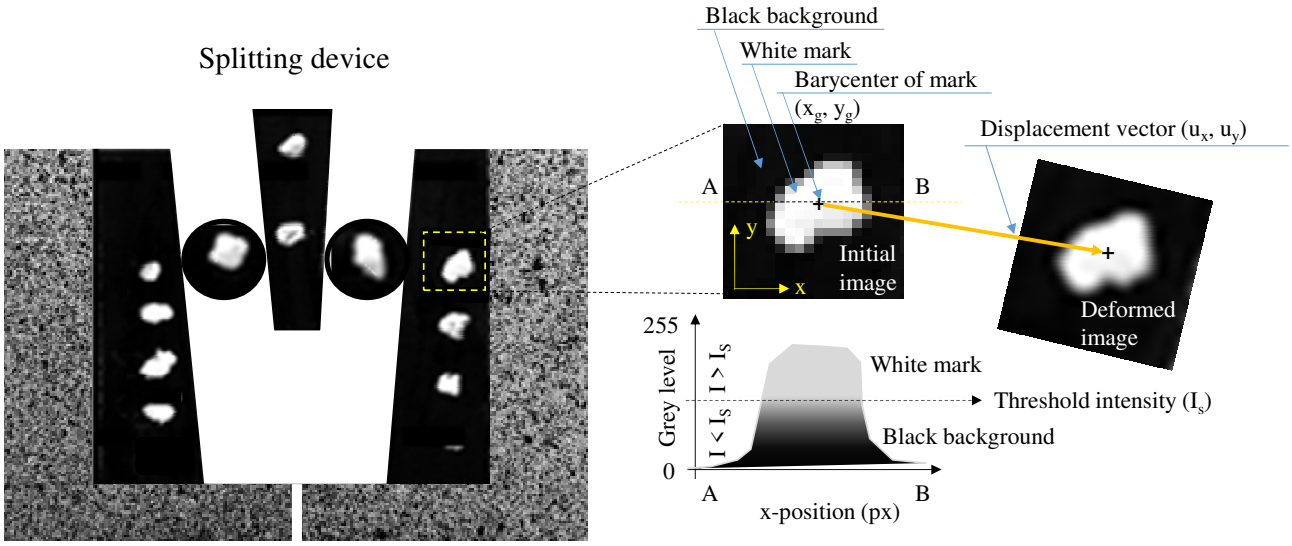

Figure 3: Principle of Mark Tracking (MT) method applied for displacement monitoring of metallic loading parts.

Within each area corresponding to a mark, I_i is the grey level of each pixel i, I_s the threshold defined by the user to proceed to the calculations only for pixels above this threshold. Then for each mark, a barycenter position (x_g, y_g) can be calculated from each pixel position weighed by their individual grey levels according to the following equations:

$$\begin{cases} x_g = \frac{\sum_i x_i (I_i - I_S)}{\sum_i (I_i - I_S)} \\ y_g = \frac{\sum_i y_i (I_i - I_S)}{\sum_i (I_i - I_S)} \end{cases} \quad (6)$$

Where (x_i, y_i) are pixel coordinates.

II.3.b. Crack opening displacement measured by Digital Image Correlation

Digital Image Correlation (DIC) is actually widely used for displacement field determination in mechanic research field [42–46]. DIC is based on the analysis of successive images of a specimen surface during a mechanical test. It consists of matching reference (f) and deformed (g) 2D images based on their grey level distribution. By assuming the conservation of the optical flow, a local plane material transformation ϕ links coordinates of the reference state ($\underline{X}$) to those of the deformed state ($\underline{x}$), by the transformation $\underline{x} = \phi(\underline{X})$. The transformation ϕ is locally defined for each subset centred on a grid of points and delimited by a zone of interest (ZOI). This local transformation is approximated by a first-order Taylor development, summarised in the vector $\underline{q} = (u, v, \frac{\partial u}{\partial x}, \frac{\partial u}{\partial y}, \frac{\partial v}{\partial x}, \frac{\partial v}{\partial y})$, which has two components of displacement (u, v) and four components of local displacement gradients.

A correlation coefficient C, expressed in equation (7) and corresponding to a Zero Normalized Cross Correlation (ZNNC) criterion, is used to find the best values for the unknown vector $\underline{q}$

components according to an optimisation procedure. Subpixel bilinear interpolation of grey levels of g is used to achieve subpixel displacement measurement.

$$C = 1 - \frac{\sum_{X\in D}(f(X)-\bar{f}_D).(g(\phi(x))-\bar{g}_D)}{\sqrt{\sum_{X\in D}(f(X)-\bar{f}_D)^2}.\sqrt{\sum_{X\in D}(g(\phi(x))-\bar{g}_D)^2}} \quad (7)$$

Where $\bar{f}_D$ and $\bar{g}_D$ are the average grey level values on subset D in the reference and in the deformed state respectively.

The strain field can then be calculated by finite differences from four adjacent subsets forming a square using the measured displacement field. In the present study, DIC is only used to measure the imposed displacement within the ROI-1 in order to quantify the Crack Opening Displacement (COD) value. These measurements were performed by using only two subsets disposed horizontally on both side of the notch with dimensions of 64x64 px^2 and a spacing of 502 px (corresponding to 29.4 mm).

II.3.c. 2 Parts Digital Image Correlation: 2P-DIC

In previous studies [47], DIC was used to follow crack propagation, but the pertinence of such approach is questionable since material transformation is no longer homogenous when crack occurs locally. That is why a Refined Digital Image Correlation algorithm (named 2P-DIC) has been used in the present case [38]. In this technique, the subset D can be split (Figure 4) at the position X_C in two parts D_1 ($x < XC$) and D_2 ($x > XC$) with an orientation θ of the boundary.

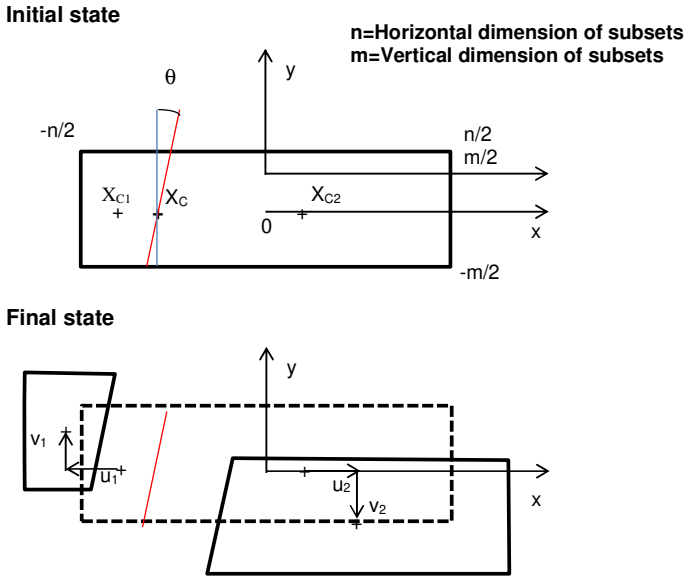

Figure 4: Principle of the 2P-DIC, decomposition of a subset in two parts.

X_C varies with increments of one pixel, between -n/4 and n/4, while θ varies, between -50° and 50°, with a pitch of 2°. In a same way than DIC process, a correlation coefficient is calculated according to Eq. 8.

$$C_{XC}(X_c, \theta, \underline{Q}) = \sum_{D_1} c^2(\underline{q_1}) + \sum_{D_2} c^2(\underline{q_2}) \quad (8)$$

Where $\underline{q_i} = \left(u_i, v_i, \frac{\partial u_i}{\partial x}, \frac{\partial u_i}{\partial y}, \frac{\partial v_i}{\partial x}, \frac{\partial v_i}{\partial y}\right)$, the vector of local material transformation parameters in the part D_i (i=1,2) while the vector $\underline{Q}$ represents all kinematic unknowns of D and is the gathering of two vectors $\underline{q_1}$ and $\underline{q_2}$

The correlation coefficient, $C_{XC}(X_c, \theta, \underline{Q})$, is minimised in order to find optimal values of $\underline{Q}$. In order to minimize the calculation time, a Normalized Sum of Squared Difference (NSSD) criterion [44] has been used, which allows the time of calculation to be reduced to a quarter of that compared to ZNNC, without decreasing the uncertainty.

In order to discriminate physical discontinuities from noise, a pseudo-strain threshold (ε) is calculated and applied according to eq. 9.

$$\varepsilon = \frac{\sqrt{(XC_2 - XC_1 + u_2 - u_1)^2 + (v_2 - v_1)^2}}{XC_2 - XC_1} - 1 \quad (9)$$

This local pseudo-strain relates directly to crack opening displacement divided by initial distance between the 2 subset parts.

Pseudo strain threshold value is then chosen by taking into account 2P-DIC technique accuracy and material behaviour. Here the value of strain measurement uncertainty is unfortunately, as in most cases, higher than the starting point of diffuse cracking within the material. Thus ε_{Thres} is determined by a preliminary protocol that consists of determining, by classical DIC, the maximum error of the strain obtained for a series of images recorded before the beginning of the mechanical test (the strain there being theoretically null without any loading). In this case, the same parameters have to be used for DIC and 2P-DIC : same subset size and ZOI.

In the present study, 2P-DIC is applied on ROI-2 to monitor crack propagation within the FPZ of the wedge splitting sample during loading. These measurements were performed by using small overlapping subsets with dimensions of 64x16 px^2 and a spacing of 32x8 px^2 in order to increase measurement spatial resolution while maintaining a good accuracy.

III. RESULTS

III.1. Measurement of crack opening displacement using optical methods

The WST setup involves an intricate interaction of metallic pieces that induces parasitic displacements. Indeed, with contact pressure evolution, small surface irregularities and roughness are sufficient to generate unwanted displacements between the metallic pieces, especially at the beginning of loading. Therefore, the measurement of the COD from the vertical load-point displacement, taking into account the angle of the wedge, usually leads to significant error resulting from the evolution of these surface contacts between metallic loading parts.

Thus, optical methods such as DIC and Mark Tracking may be used as a convenient way to fully monitor WST setup displacements and determine the crack opening displacement accurately. The measurement setup used in this study is presented in Figure 1 where both markers and a speckle pattern are used as a measurement basis for the application of the MT method and DIC, respectively.

In order to analyse WST setup behaviour during an experiment, different measurement points have been followed throughout loading of a refractory sample. Firstly, the vertical displacements of the crosshead, of the wedge and of the rolls were measured and plotted in Figure 5a.

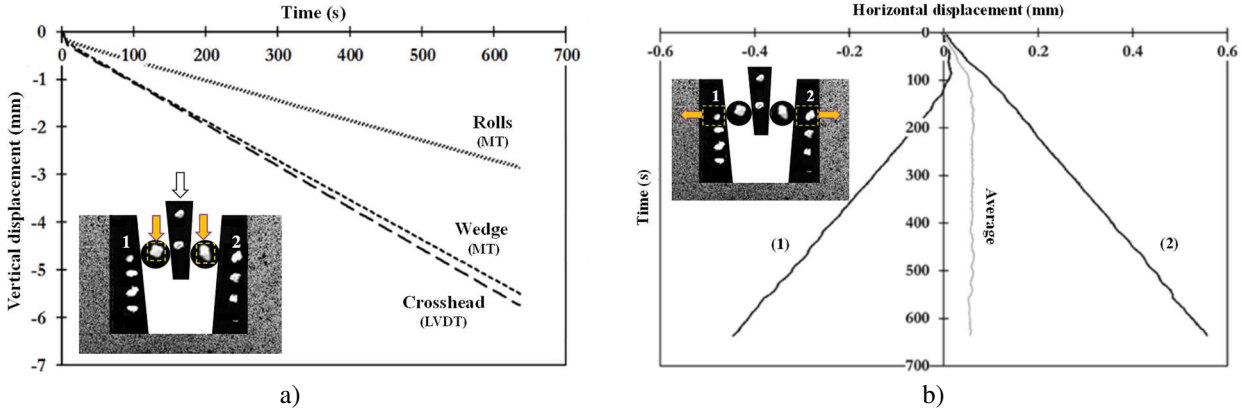

Figure 5: Monitoring of loading parts by Mark Tracking during a WST: a) vertical displacement of the crosshead, of the wedge and of the two rolls versus time, b) horizontal displacements of Mark 1 and 2 deposited on the two metallic supports and average of these supports displacements.

The vertical displacements of the crosshead and the wedge are on a comparable level, while roll displacements are significantly lower. In fact, due to rolling movement on these rolls, their

displacements are logically half of the displacement of the wedge. In addition, one could notice that the vertical displacement of the wedge is slightly lower than the displacement of the machine crosshead. More interestingly, Figure 5b reports horizontal displacements of two markers (Marks 1 and 2) located on the metallic supports on each side of the groove versus time (on Y axis). These last results reveal a slight rotation of the sample around the linear support at the beginning of loading as both markers shift towards the right in the early stage of the test. Given that no pre-load had been applied, contact between WST setup parts is not achieved from the beginning and may, therefore, lead to parasitic displacements. Nevertheless, the average value of marker displacements remains constant after about 100 s, albeit with the presence of some negligible measurement noise, suggesting that markers on metallic supports may be used for crack opening displacement determination.

In order to determine the most accurate way to measure crack opening displacement during a WST, displacements were compared between markers placed on the metallic supports, subsets placed close to the border of the sample and horizontal displacements deduced from the vertical displacement of the wedge. For the measurement of displacements using DIC, large subsets on each side of the sample, as shown in Figure 1, were chosen to ensure that measurement accuracy is optimal. The evolution of these measurement points has been reported in Figure 6 as a function of time.

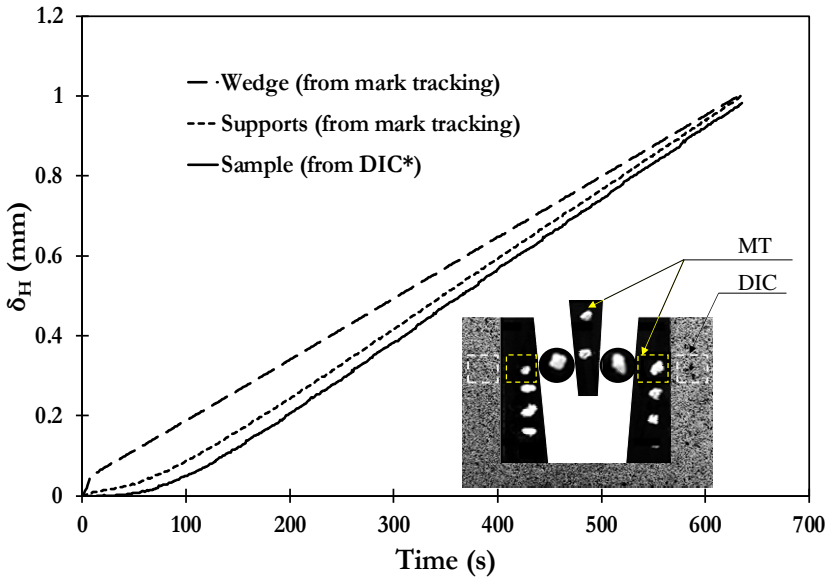

Figure 6: Evolution of crack opening displacement δ_H versus time during a WST, which can be obtained from the vertical displacement of the wedge (Wedge), from markers placed on the two metallic supports (Supports) and from subsets placed close to the border of the sample (Sample).

In order to complement this analysis, some differences have been specifically calculated using COD directly measured on sample by DIC as reference. Figure 7 reports thus the difference between this reference and the COD values deduced from the wedge's vertical displacement as well as the one obtained from the 2 marks on the supports.

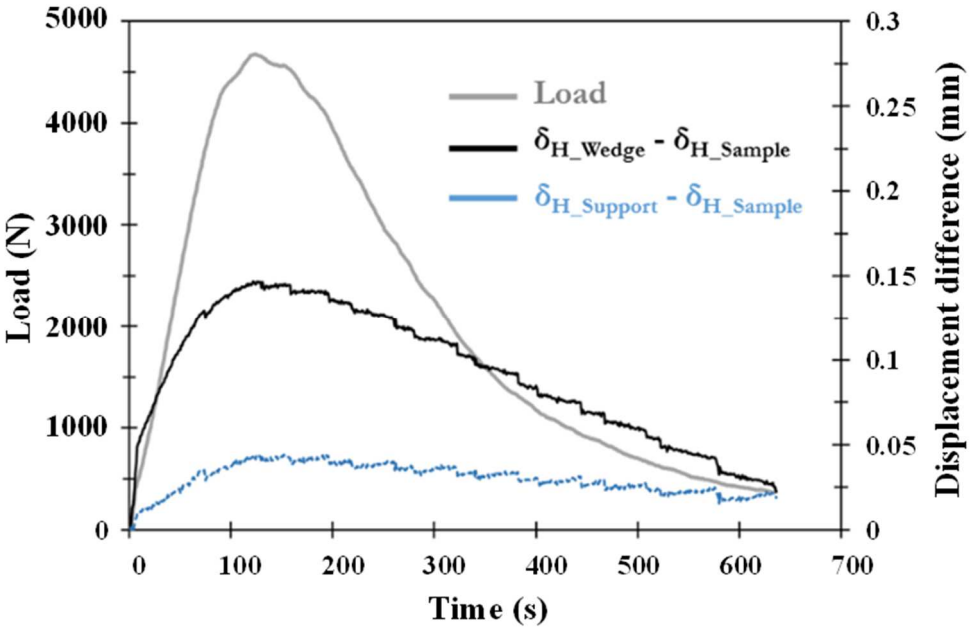

Figure 7: Difference in crack opening displacement δ_H versus time during a WST, between Wedge and Sample methodologies, and between Support and Sample methodologies.

One could notice that COD values from marks deposited on supports are obviously closer to reference values obtained by DIC directly on sample, in comparison to values obtained classically from wedge vertical displacement (Eq. 2), which are in fact far away from true COD values, especially at maximum load (just before final rupture). In fact, interestingly, these curves on Figure 7 demonstrate that the investigated errors are strongly connected to the load level (peak of these curves corresponding to maximum load). These results suggest that prior to the peak load, metallic part displacement rates are higher than that of the sample. This is most likely due to contact pressure between the metallic parts along with imperfect surface contacts between these parts and the sample. Therefore, as illustrated in Figure 8, when COD measurement are not managed directly on the sample, an artificial curvature is obtained at the beginning of loading, which is believed to be directly related to the evolution of these contacts .

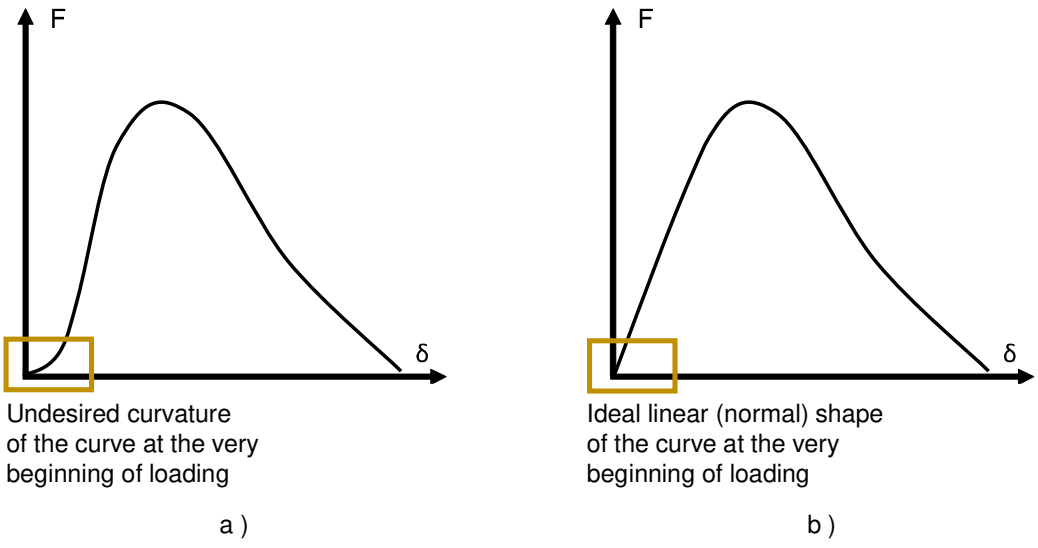

Figure 8: Horizontal load versus COD during WST: deduced from Wedge vertical displacement (a) and measured directly by DIC on the sample (b).

This preliminary study on the COD measurement shows very well the great impact of the boundary conditions and the importance of considered measurement points. These aspects are very important, as the relevance of the analysis of the fracture process depends on them. Consequently, the crack opening displacement is best measured directly on the sample, by using DIC method.

III.2. Crack detection by 2P-DIC

III.2.a. Measurement of the main crack path and fracture process zone features

Crack length can be measured according to two methods. The first, defined as an equivalent crack length, considers crack length as a straight line going from the root of the notch to the vertical position of the bottom-most subset that contains a crack. This "classical" approach, commonly used in the literature, does not take into account the multi-damage aspects that can be observed during the crack propagation. The second corresponds to damage length as it measures the sum of all vertical or inclined subset segments affected by a discontinuity, including all crack features including deviations and secondary branches, which are common patterns in quasi-brittle refractories. Figure 1 illustrates both crack lengths obtained thanks to the coupling of WST and 2P-DIC.

Nevertheless, it has been observed through WST experiments that damage length evolution as a function of images, or time, is not always increasing, as reported in Figure 9. Indeed, crack length from state t_i can be higher than crack length at state t_{i+1}, which is not in accordance with the definition of a crack. This measurement artefact is due to the principle of discontinuity detection in 2P-DIC (and DIC methods in general) which is based on strain value thresholding, thus if a local strain value corresponding to a crack in t_i decreases in t_{i+1}, the discontinuity disappears from a numerical point of view. Local strain decrease is justified, and especially observed using 2P-DIC, when secondary cracks are away from the main crack tip during unloading because of stress decrease in the crack wake region [48].

Therefore, a cumulated damage length concept has been introduced, which curbs this measurement artefact as shown in Figure 9.

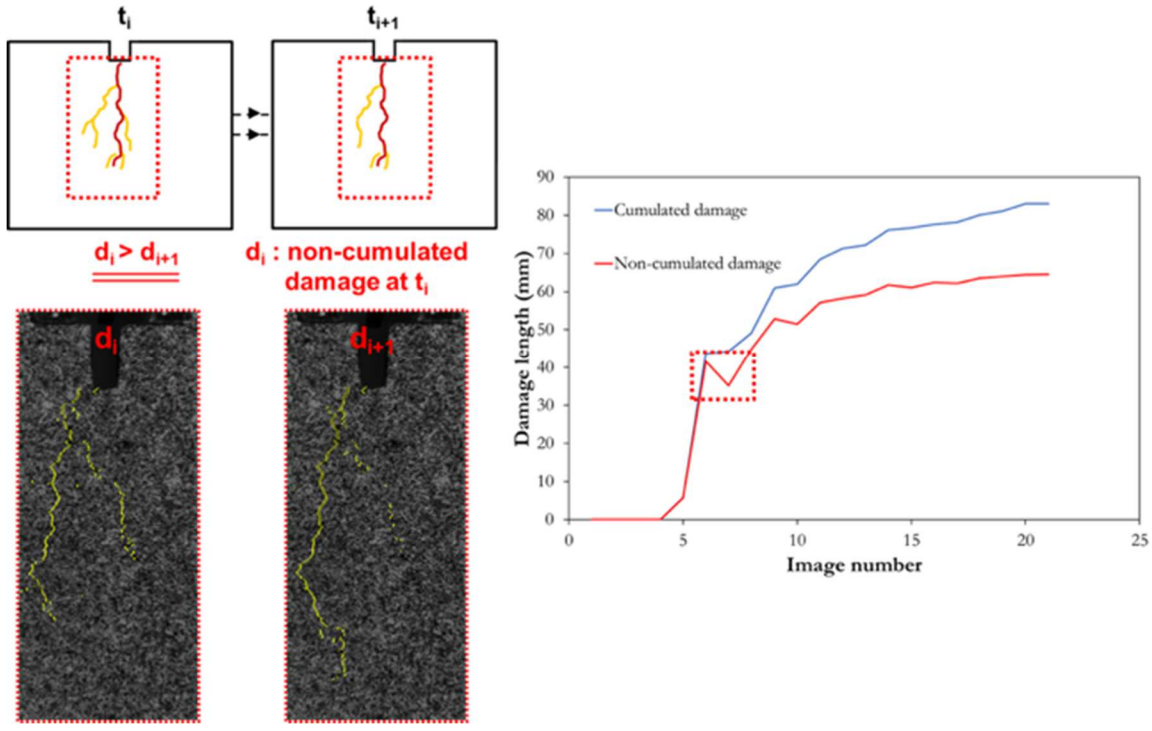

Figure 9: Example of local strain decrease leading to artificial crack closure during a WST and cumulated damage measured by 2P-DIC which is not affected.

As a result, the cumulated damage length takes into account all of the cracks that may have appeared during the WST experiment. This parameter will be used to highlight the degree of cracking during a WST and compared with the equivalent crack length in an attempt to understand the impact of the FPZ.

Thanks to the 2P-DIC crack detection principle, an increased crack spatial resolution can be compared with standard DIC. Indeed, crack position (given by XC value) is defined with an uncertainty equal to one pixel, which is not the case for standard DIC. This increased spatial resolution leads to a finer description of crack edges and deviations, the extent of which will be evaluated in the next section.

III.2.b. Comparison with post-mortem SEM observations

In order to validate crack length measurement by 2P-DIC experimentally, a post-mortem observation was performed on a WST sample to compare crack features and length between 2P-DIC and SEM observations.

Therefore, a cylinder with a diameter of 30 mm was machined from the upper part of the cracked area, just below the notch in the post-mortem WST sample, 25 mm of which contains the crack. The same sample surface used for 2P-DIC measurements was prepared for SEM observations to ensure a proper comparison. Therefore, the painted layer used as a speckle was first removed and then successive steps of polishing were undertaken using relatively fine grained polishing paper to prepare a planar surface for SEM. Observations were then carried out and images were acquired then assembled to form one global image containing the whole 25 mm of the cracked sample. The global image is then treated using a series of image analysis tools to extract the main crack path and ignoring the secondary crack branches.

The global image is then treated using a series of image analysis tools to extract the main crack path and ignoring the secondary crack branches. The image treatment protocol is summarised in Figure 10.

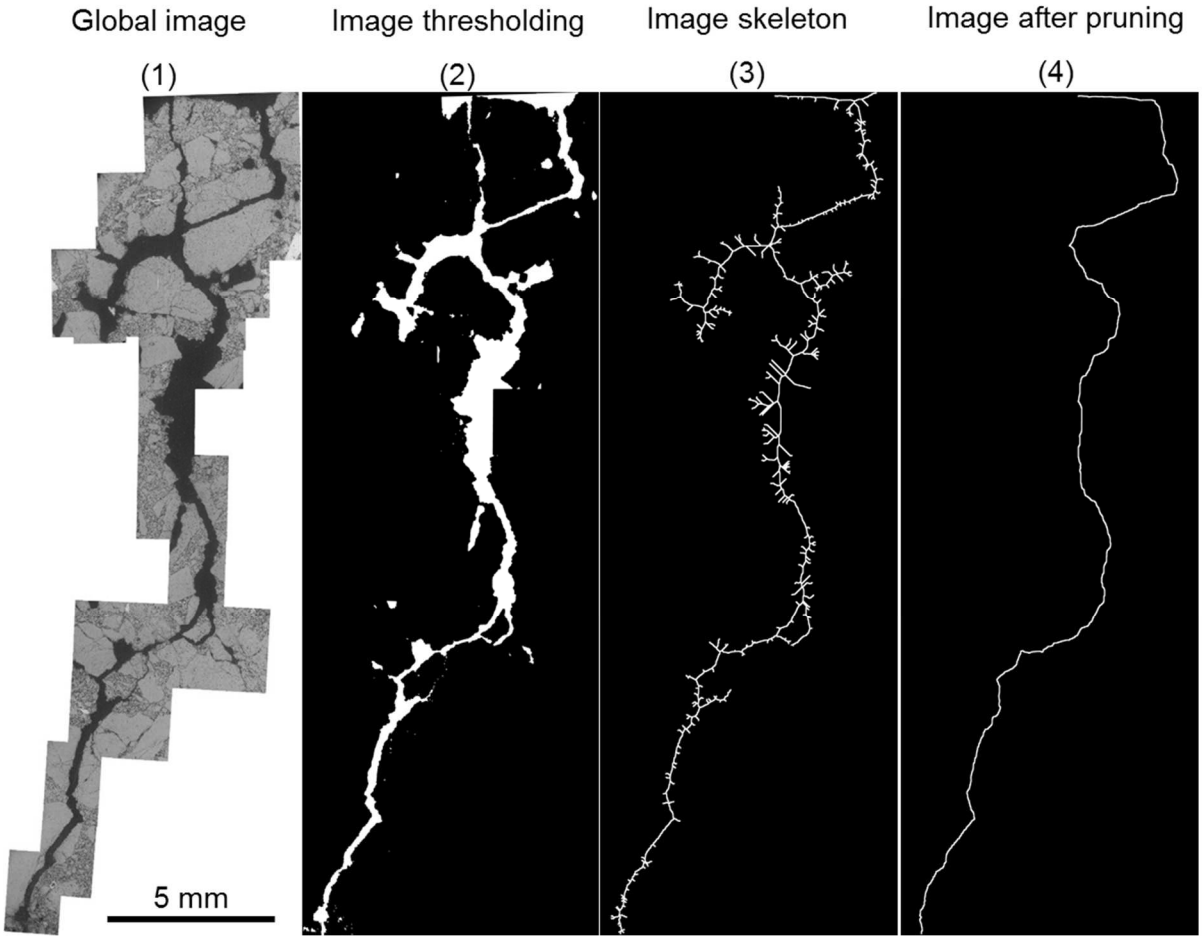

Figure 10: Global SEM image analysis steps to extract the main crack path

Once the crack path is obtained, the length is measured and then compared with the 2P-DIC image. As shown in Figure 11, the main crack deviations are highlighted by blue dashed horizontal lines between the SEM and 2P-DIC image. As a first observation, the 2P-DIC image follows the same trend as that observed by SEM but some subsets come short of being linked to others due to insufficient inclination limited by the 2P-DIC algorithm. Nevertheless, the overall outcome of 2P-DIC is very close to the post-mortem sample observed under SEM. In fact, the crack length measured on the global SEM image was estimated at 31.5 mm while the 2P-DIC crack measures 28.7 mm, which is a rather small difference.

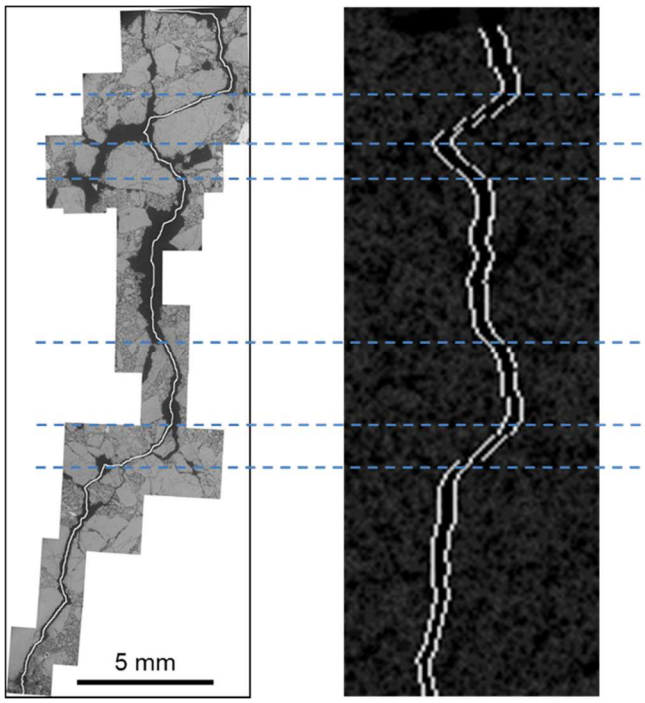

Figure 11: Comparison of SEM observation of post-mortem WST sample and 2P-DIC image of the same sample during the WST.

Therefore, 2P-DIC detects the main crack path with a very good accuracy as suggested by the comparison with post-mortem SEM observations. This validates the reliability of 2P-DIC as a method to measure crack lengths during fracture experiments such as the WST, which will be used to enrich fracture characterisation. Ultimately, 2P-DIC provides ways to refine the understanding of the fracture behaviour of quasi-brittle refractory materials.

III.3. Estimation of crack propagation resistance curves

Fracture experiments were performed using a crosshead speed of 0.5mm/min on pure magnesia and magnesia-spinel composites containing 5% of spinel aggregates. The latter is known to exhibit reduced brittleness due to existing microcrack networks within the microstructure as a result of thermally induced stresses during cooling after sintering.

In the current analysis, fracture energy was calculated at each loading state of the WST using the corresponding crack length measured by 2P-DIC. The objective of this approach is to evaluate the evolution of the crack propagation resistance of a material and, to a certain extent, the impact of FPZ development on fracture energy.

Given that two crack lengths can be measured using 2P-DIC, it is possible to calculate two fracture energies. As such, an equivalent fracture energy ($G_{eq,i}$) has been defined according to the following equation.

$$G_{eq,i} = \frac{1}{L_{eq,i}.B}\left(\int_0^{\delta_{H,i}} F_H \,.\, d\delta_H - \frac{1}{2}.F_H\delta_H\right) \quad (10)$$

Where $L_{eq,i}$ is the equivalent crack length measured by 2P-DIC at a specific loading state i. As a reminder, this length corresponds to a straight crack going down from the bottom of the notch to the detected crack tip and B is the thickness of the WST sample.

Moreover, an effective fracture energy, based on the cumulated damage length can be calculated according to Eq. 11.

$$G_{eff,i} = \frac{1}{L_{eff,i}.B}\left(\int_0^{\delta_{H,i}} F_H \,.\, d\delta_H - \frac{1}{2}.F_H\delta_H\right) \quad (11)$$

Where $L_{eff,i}$ is the cumulated damage length measured by 2P-DIC at a specific loading state i. Figure 12 shows the evolution of equivalent fracture energy as a function of equivalent crack length throughout the entire duration of the WST. The grey area at the beginning of loading has been deliberately disregarded due to an unstable evolution of energy. The curves exhibit an increasing trend that is generally associated with the rising R-curve effect reported in materials with toughening mechanisms.

The pure MgO material exhibits a rather stable plateau evolution of equivalent fracture energy with a slightly increasing trend as function of equivalent crack length. However, for MH5 an unstable evolution of fracture energy, instead of a plateau evolution followed by a rise in energy, can be observed.

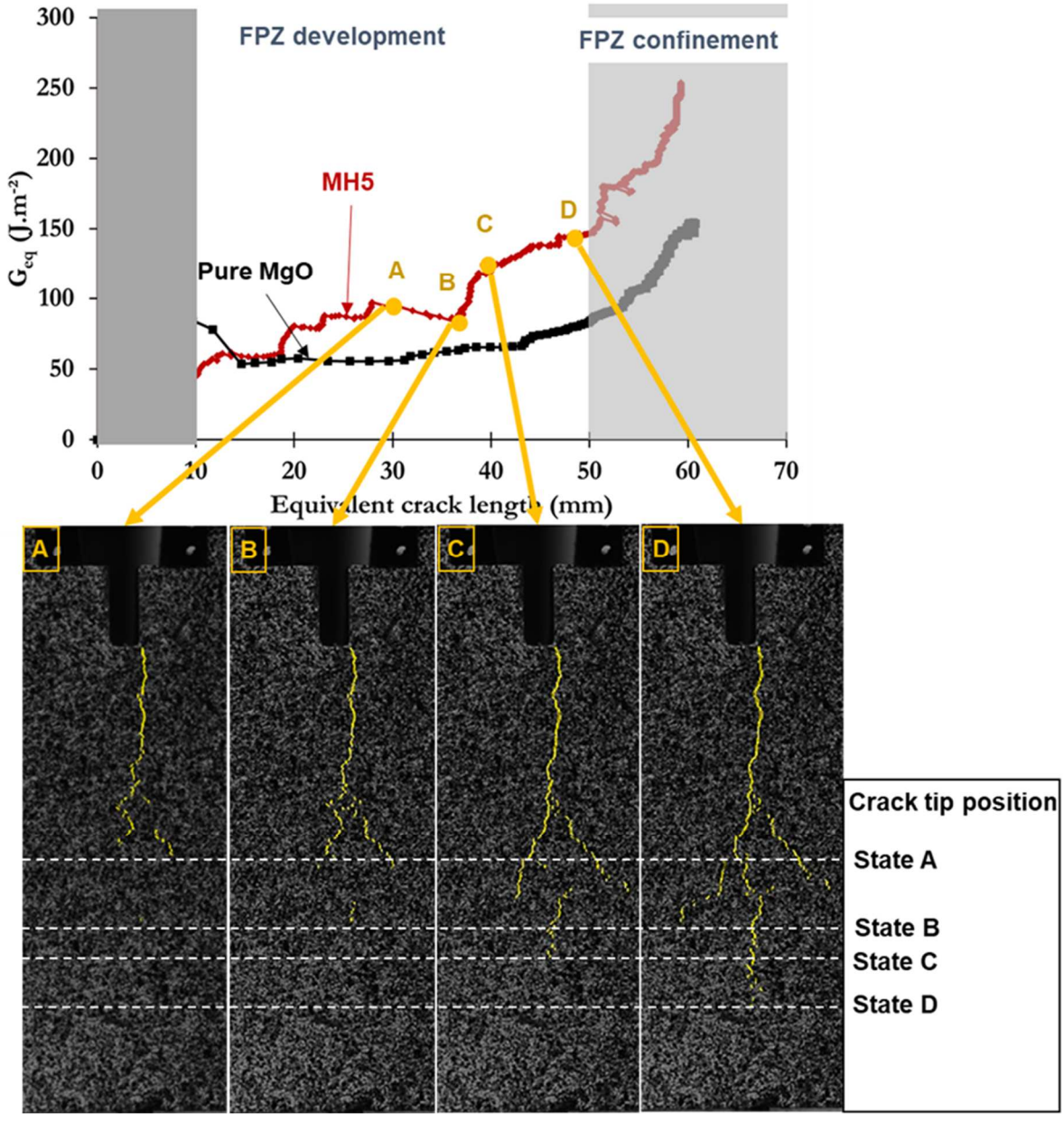

Figure 12: Evolution of equivalent fracture energy (G_{eq}) as a function of equivalent crack length for MgO and MH5, with 2P-DIC images illustrating multiple cracking in MH5.

This unstable evolution is driven by repeated sudden increases in energy that can be observed during most of the experiment for MH5, as opposed to pure MgO. In order to understand the origin of these energy jumps exhibited by MH5, specific loading states (A-B-C-D) have been conveniently chosen on the curve. In each of these states, images showing cracking features as measured by2P-DIC are displayed below the graph. Dashed lines have been added at the crack tip that was detected by 2P-DIC and used to measure equivalent crack length in order to highlight its evolution between the different states. As a reminder, equivalent crack length measures the distance between the notch root and the crack tip detected by 2P-DIC as a vertical straight line. Therefore, this length does not take into account other cracks features such as crack deviation and branching. From state A to state B, a slight decrease of equivalent fracture energy (in J/m^2) can be observed since equivalent crack length increases (linked to surface area in m^2) at a higher rate in comparison to energy consumption (in J). The occurrence of a crack in state B that is distant from the crack tip in state A suggests that there is a process zone (not visible on the present image B), which is large enough, in front of the initial crack tips (on state A) where diffuse damage might take place. Nonetheless, a decrease in equivalent fracture energy is observed from A to B, but this decrease results from the way in which crack length is measured here by 2P-DIC (equivalent crack length). In fact, equivalent crack length takes, in this case, mainly into account the occurrence of the small crack which occur far from the two initial one in state A.

In the next stage, from B to C, the original crack branches (already observed in state A), continue their advance while the crack in the middle, which is distant from the branches, grows at the same time toward the bottom and the top. From state B and C, it can be easily observed that the cumulated length increase of cracks is higher than from state A to B. Moreover, the equivalent crack length evolution, which corresponds to crack tip advancement, is relatively small, as highlighted by the dashed lines. Consequently, the cumulated length increase is much higher than the advancement of the main crack's tip , leading to a lower evolution of equivalent crack length compared to energy consumption. Indeed, as shown on the graph, fracture energy increases at a high rate between states B and C. The limited growth of the main crack tip and the growth of cracks in the wake region lead to this increase of fracture energy. This analysis strongly suggests that FPZ, and especially crack growth in the wake region, lead to an increase of the consumed fracture energy and slows the growth of the main crack. Finally, from state C to D, crack growth continues, both at the main crack tip and in the wake region, where the two crack branches have continued their growth. In fact, the crack branch on the left created another branch with the main crack tip. These images, obtained thanks to 2P-DIC measurements, show just how intricate FPZ interactions take place during stable fracture experiments. Finally, when the bottom of the sample is reached at the end of the experiment, an exponential increase of fracture energy occurs. This effect is mostly related to the confinement of the FPZ by the compressive zone at the bottom of the WST sample. In fact, the increase starts well before the end of the experiment around an equivalent crack length of 50 mm due to the large size of the compressive zone. Therefore, geometric and experimental constraints lead to a difficult estimation of crack propagation resistance, especially when a large FPZ is developed.

Ultimately, the analysis of equivalent fracture energy evolution demonstrated successive FPZ developments, as shown in the 2P-DIC images of Figure 12 for MH5. These FPZ related phenomena are purposely not taken into account in the equivalent crack length thus leading to an abrupt increase of energy.

While the evolutions of equivalent fracture energy hint strongly at FPZ developments during the WST, the unstable character of the curves impedes the observation of the characteristic R-curve plateau after an initial increase of fracture energy. Nevertheless, the influence of FPZ development on fracture energy can clearly be highlighted on MH5, compared to pure MgO. In this sense, a stable plateau can be expected by taking into account all damage coming from the FPZ using the cumulated damage length measured by 2P-DIC.

Indeed, by calculating the effective fracture energy, a much more stable plateau can be observed in Figure 13 after an initial increase at the beginning of the WST. Then, at the end of the experiment, fracture energy increases due to FPZ confinement coming from the action of the compressive zone at the bottom of the sample.

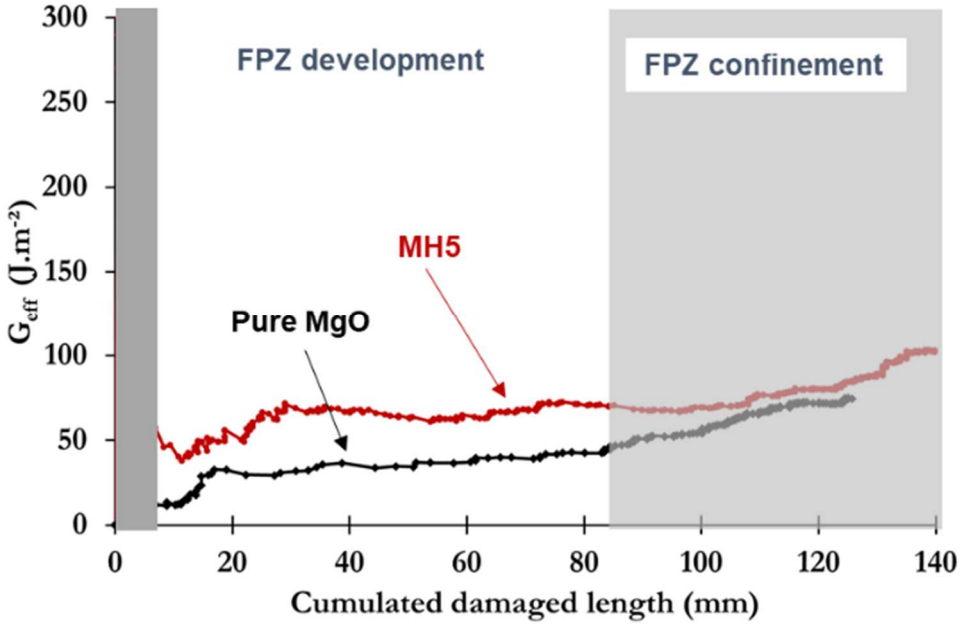

Figure 13: Evolution of equivalent fracture energy (G_{eq}) as a function of cumulated damaged length for MgO and MH5.

With such analytical treatment (considering cumulated damaged length), both pure MgO and MH5 exhibit in fact rather similar trends (an initial increase followed by a rather constant value). Nevertheless, the value of fracture energy at the plateau seems significantly higher for MH5 (about 70 J.m^{-2}) in comparison to pure MgO (about 30 J.m^{-2}). In general, such low values result from the integration within the considered overall cracked surface of all microcracks resulting from FPZ and here detected by 2P-DIC. Additionally, higher value of effective fracture energy for MH5 (well-known to contain numerous initial microcracks around hercynite inclusions) could results from very small microcracks evolutions during loading (diffused damage) that cannot be detected today by 2P-DIC technique.

In essence, fracture energy values could be as low as a few J.m^{-2}, in accordance with the surface energies of the studied materials.

The present analysis underlined the characteristic rising R-curve behaviour that is associated with the full development of the FPZ and its wake. By using 2P-DIC to measure crack propagation features such as multiple-cracking and effective fracture energies could be measured for the materials with great accuracy. Nevertheless, given the nature of the material microstructures, especially that of hercynite containing materials, it appears quite clearly that a single measurement at macro-scale is not sufficient to account for all cracking features that consume energy. Ultimately, the R-curve approach makes use of the full potential of 2P-DIC in measuring the evolution of crack propagation resistance, which is an essential material property.

IV. CONCLUSION

Thermal shock loading can lead to critical consequences for a refractory installation if material properties are not chosen accordingly. In order to improve the ability of refractory materials to sustain thermal shocks, an increased strain-before-fracture and a high level of fracture energy may be used as microstructure design criteria. Hence, materials with a non-linear mechanical behaviour, also known as “flexible” materials, can be considered. For instance, voluntarily introducing a network of microcracks in the initial material microstructure promotes energy dissipating mechanisms during loading, which increases the overall material strain while limiting crack extension.

Model materials composed of Magnesia and Hercynite have been investigated in the present study in order to understand the impact of energy dissipating mechanisms on fracture process zone (FPZ) development and the fracture behaviour. In order to better understand the phenomena taking place during fracture, simplified compositions of two types of refractories have been elaborated namely a pure Magnesia material and a Magnesia-Hercynite composite.

The fracture behaviour of 2 model materials has been evaluated accurately by coupling the WST with DIC. Strength and fracture energy values highlight some clear differences between these 2 materials and indicate strong trends regarding the influence of hercynite inclusions dispersed within the magnesia matrix. As such, the introduction of hercynite inclusions leads to a decrease of strength while increasing fracture energy. This impact has been attributed to the presence of an initial microcrack network within model materials containing hercynite inclusions, which leads to the development of a large FPZ that consumes energy during crack propagation.

Indeed, the influence of the FPZ has been identified in magnesia-hercynite materials by using the 2P-DIC method, which revealed the presence of a multiple cracking zone. This process related to the coalescence of micro-cracking network and the material microstructure is responsible for a large part of the consumed energy during fracture as they lead to the creation of many crack surfaces.

In a more refined analysis, the R-curve approach has been used to provide additional insight on FPZ development in conjunction with the respective microstructures of pure magnesia and magnesia-hercynite materials. By following the evolution of an equivalent fracture energy and an effective one, defined using the different crack lengths measured by 2P-DIC, the impact of multiple cracks on the consumed energy was clearly shown. In fact, given the presence of a diffusion zone in magnesia-hercynite materials leading to fine microcracks, higher fracture energies were observed for materials containing hercynite.

Up to now, such deep investigations combining WST with 2P-DIC have been possible only at room temperature. Of course, it could be of interest to investigate such behaviour also at high temperature. This requires the development of dedicated speckle patterns which can allow accurate strain field measurements at high temperature by 2P-DIC. Such developments have been recently achieved, which will soon allow similar tests to be managed in temperature conditions close to those used during the application of refractories.

ACKNOWLEDGEMENT

This study was conducted within the framework of FIRE (Federation of International Refractory Research and Education) project Delta. RHI-Magnesita is gratefully acknowledged for providing materials for the study.

REFERENCES

[1] Hasselman D P H 1969 Unified Theory of Thermal Shock Fracture Initiation and Crack Propagation in Brittle Ceramics *J. Am. Ceram. Soc.* **52** 600–4

[2] Hasselman D P H 1963 Elastic Energy at Fracture and Surface Energy as Design Criteria for Thermal Shock *J. Am. Ceram. Soc.* **46** 535–40

[3] Gogotsi G A, Groushevsky Ya L and Strelov K K 1978 The significance of non-elastic deformation in the fracture of heterogeneous ceramic materials *Ceramurg. Int.* **4** 113–8

[4] Harmuth H, Rieder K, Krobath M and Tschegg E 1996 Investigation of the nonlinear fracture behaviour of ordinary ceramic refractory materials *Mater. Sci. Eng. A* **214** 53–61

[5] Larson D R, Coppola J A, Hasselman D P H and Bradt R C 1974 Fracture Toughness and Spalling Behavior of High-Al2O3 Refractories *J. Am. Ceram. Soc.* **57** 417–21

[6] Evans A G 1990 Perspective on the Development of High-Toughness Ceramics *J. Am. Ceram. Soc.* **73** 187–206

[7] Budiansky B, Amazigo J C and Evans A G 1988 Small-scale crack bridging and the fracture toughness of particulate-reinforced ceramics *J. Mech. Phys. Solids* **36** 167–87

[8] Evans A G and Faber K T 1984 Crack-Growth Resistance of Microcracking Brittle Materials *J. Am. Ceram. Soc.* **67** 255–60

[9] Lange F F 1979 Fracture Toughness of Si3N4 as a Function of the Initial α-Phase Content *J. Am. Ceram. Soc.* **62** 428–30
[10] Amazigo J C and Budiansky B 1988 Interaction of particulate and transformation toughening *J. Mech. Phys. Solids* **36** 581–95
[11] Harmuth H, Rieder K, Krobath M and Tschegg E 1996 Investigation of the nonlinear fracture behaviour of ordinary ceramic refractory materials *Mater. Sci. Eng. A* **214** 53–61
[12] Huger M, Ota T, Tessier-Doyen N, Michaud P and Chotard T 2011 Microstructural effects associated to CTE mismatch for enhancing the thermal shock resistance of refractories *IOP Conf. Ser. Mater. Sci. Eng.* **18** 222002
[13] Selsing J 1961 Internal Stresses in Ceramics *J. Am. Ceram. Soc.* **44** 419–419
[14] Tessier-Doyen N, Glandus J C and Huger M 2006 Untypical Young's Modulus Evolution of Model Refractories at High Temperature *J. Eur. Ceram. Soc.* **26** 289–95
[15] Aksel C, Rand B, Riley F L and Warren P D 2004 Thermal shock behaviour of magnesia–spinel composites *J. Eur. Ceram. Soc.* **24** 2839–45
[16] Aksel C, Rand B, Riley F L and Warren P D 2002 Mechanical properties of magnesia-spinel composites *J. Eur. Ceram. Soc.* **22** 745–54
[17] Ghosh A, Sarkar R, Mukherjee B and Das S K 2004 Effect of spinel content on the properties of magnesia–spinel composite refractory *J. Eur. Ceram. Soc.* **24** 2079–85
[18] Grasset-Bourdel R, Alzina A, Huger M, Chotard T, Emler R, Gruber D and Harmuth H 2013 Tensile behaviour of magnesia-spinel refractories: Comparison of tensile and wedge splitting tests *J. Eur. Ceram. Soc.* **33** 913–23
[19] Griffith A A and Gilman J J 1968 The phenomena of rupture and flow in solids *Trans. ASM* **61** 855–906
[20] Bažant Z P and Kazemi M T 1991 Size dependence of concrete fracture energy determined by RILEM work-of-fracture method *Int. J. Fract.* **51** 121–38
[21] Bazant Z P and Planas J 1997 *Fracture and Size Effect in Concrete and Other Quasibrittle Materials* (CRC Press)
[22] Brühwiler E and Wittmann F H 1990 The wedge splitting test, a new method of performing stable fracture mechanics tests *Eng. Fract. Mech.* **35** 117–25
[23] Ebrahimi M E, Chevalier J and Fantozzi G 2003 R-curve evaluation and bridging stress determination in alumina by compliance analysis *J. Eur. Ceram. Soc.* **23** 943–9
[24] N. Cunha-Duncan F and C. Bradt R 2003 Fracture of refractories *Cerâmica* **49** 199–215
[25] Palmer G B and Baker G 1993 A load-cycling technique for R-curve behaviour: application to a low cement refractory *Int. J. Fract.* **62** 233–44
[26] Sakai M, Yoshimura J-I, Goto Y and Inagaki M 1988 R-Curve Behavior of a Polycrystalline Graphite: Microcracking and Grain Bridging in the Wake Region *J. Am. Ceram. Soc.* **71** 609–16
[27] Sakai M and Bradt R C 1993 Fracture toughness testing of brittle materials *Int. Mater. Rev.* **38** 53–78
[28] Sakai M and Bradt R C 1986 Graphical Methods for Determining the Nonlinear Fracture Parameters of Silica and Graphite Refractory Composites *Fracture Mechanics of Ceramics: Volume 7 Composites, Impact, Statistics, and High-Temperature Phenomena* ed R C Bradt, A G Evans, D P H Hasselman and F F Lange (Boston, MA: Springer US) pp 127–42
[29] Salvini V R, Pandolfelli V C and Bradt R C 2012 Extension of Hasselman's thermal shock theory for crack/microstructure interactions in refractories *Ceram. Int.* **38** 5369–75
[30] Gangnant A 2016 *Étude de la rupture quasi-fragile d'un béton à l'échelle mésoscopique : aspects expérimentaux et modélisation* thesis (Bordeaux)
[31] Sutton M A, Helm J D and Boone M L 2001 Experimental study of crack growth in thin sheet 2024-T3 aluminum under tension-torsion loading *Int. J. Fract.* **109** 285–301
[32] Pop O, Dubois F and Absi J 2013 J-integral evaluation in cracked wood specimen using the mark tracking method *Wood Sci. Technol.* **47** 257–67
[33] Scorza D, Marsavina L, Carpinteri A, Ronchei C and Vantadori S 2019 Size-effect independence of particleboard fracture toughness *Compos. Struct.* **229** 111374
[34] Belrhiti Y, Huger M, Chotard T, Pop O, Germaneau A, Doumalin P and Christophe Dupré J

2014 Characterization of the Mechanical Behavior of Magnesia Spinel Refractories Using Image Correlation *Int. J. Appl. Ceram. Technol.* **11**
[35] Dai Y, Gruber D and Harmuth H 2017 Determination of the fracture behaviour of MgO-refractories using multi-cycle wedge splitting test and digital image correlation *J. Eur. Ceram. Soc.* **37** 5035–43
[36] Vargas R, Neggers J, Canto R B, Rodrigues J A and Hild F 2016 Analysis of wedge splitting test on refractory castable via integrated DIC *J. Eur. Ceram. Soc.* **36** 4309–17
[37] Dupré J C, Doumalin P, Husseini H A, Germaneau A and Brémand F 2015 Displacement Discontinuity or Complex Shape of Sample: Assessment of Accuracy and Adaptation of Local DIC Approach *Strain* **51** 391–404
[38] Dupré J-C, Doumalin P, Belrhiti Y, Khlifi I, Pop O and Huger M 2017 Detection of cracks in refractory materials by an enhanced digital image correlation technique *J. Mater. Sci.* **53**
[39] Bretagne N, Valle V and Dupré J C 2005 Development of the marks tracking technique for strain field and volume variation measurements *NDT E Int.* **38** 290–8
[40] Rotinat R, Tié R bi, Valle V and Dupré J-C 2001 Three Optical Procedures for Local Large-Strain Measurement *Strain* **37** 89–98
[41] Belrhiti Y, Gallet-Doncieux A, Germaneau A, Doumalin P, Dupre J C, Alzina A, Michaud P, Pop I O, Huger M and Chotard T 2012 Application of optical methods to investigate the non-linear asymmetric behavior of ceramics exhibiting large strain to rupture by four-points bending test *J. Eur. Ceram. Soc.* **32** 4073–81
[42] Réthoré J, Hild F and Roux S 2008 Extended digital image correlation with crack shape optimization *Int. J. Numer. Methods Eng.* **73** 248–72
[43] Wang Y Q, Sutton M A, Bruck H A and Schreier H W 2009 Quantitative Error Assessment in Pattern Matching: Effects of Intensity Pattern Noise, Interpolation, Strain and Image Contrast on Motion Measurements *Strain* **45** 160–78
[44] Bornert M, Brémand F, Doumalin P, Dupré J-C, Fazzini M, Grédiac M, Hild F, Mistou S, Molimard J, Orteu J-J, Robert L, Surrel Y, Vacher P and Wattrisse B 2009 Assessment of Digital Image Correlation Measurement Errors: Methodology and Results *Exp. Mech.* **49** 353–70
[45] Amiot F, Bornert M, Doumalin P, Dupré J-C, Fazzini M, Orteu J-J, Poilâne C, Robert L, Rotinat R, Toussaint E, Wattrisse B and Wienin J S 2013 Assessment of Digital Image Correlation Measurement Accuracy in the Ultimate Error Regime: Main Results of a Collaborative Benchmark *Strain* **49** 483–96
[46] Barranger Y, Doumalin P, Dupré J C and Germaneau A 2012 Strain Measurement by Digital Image Correlation: Influence of Two Types of Speckle Patterns Made from Rigid or Deformable Marks *Strain* **48** 357–65
[47] Belrhiti Y, Pop O, Germaneau A, Doumalin P, Dupré J C, Harmuth H, Huger M and Chotard T 2015 Investigation of the impact of micro-cracks on fracture behavior of magnesia products using wedge splitting test and digital image correlation *J. Eur. Ceram. Soc.* **35** 823–9
[48] Grasset-Bourdel R 2011 *Structure/property relations of magnesia-spinel refractories : experimental determination and simulation* thesis (Limoges)